

## HIGH-WAVENUMBER SOLAR *f*-MODE STRENGTHENING PRIOR TO ACTIVE REGION FORMATION

NISHANT K. SINGH<sup>1</sup>, HARSHA RAICHUR<sup>1</sup>, & AXEL BRANDENBURG<sup>1,2,3,4</sup>

<sup>1</sup>Nordita, KTH Royal Institute of Technology and Stockholm University, Roslagstullsbacken 23, SE-10691 Stockholm, Sweden

<sup>2</sup>JILA and Department of Astrophysical and Planetary Sciences, University of Colorado, Boulder, CO 80303, USA

<sup>3</sup>Department of Astronomy, AlbaNova University Center, Stockholm University, SE-10691 Stockholm, Sweden

<sup>4</sup>Laboratory for Atmospheric and Space Physics, University of Colorado, Boulder, CO 80303, USA

July 7, 2021, Revision: 1.318

### ABSTRACT

We report a systematic strengthening of the local solar surface or fundamental *f*-mode 1–2 days prior to the emergence of an active region (AR) in the same (corotating) location. Except for a possibly related increase in the kurtosis of the magnetic field, no indication can be seen in the magnetograms at that time. Our study is motivated by earlier numerical findings of Singh et al. (2014) which showed that, in the presence of a nonuniform magnetic field that is concentrated a few scale heights below the surface, the *f*-mode fans out in the diagnostic  $k\omega$  diagram at high wavenumbers. Here we explore this possibility using data from the Helioseismic and Magnetic Imager on board the *Solar Dynamics Observatory* and show for six isolated ARs, 11130, 11158, 11242, 11105, 11072, and 11768, that at large latitudinal wavenumbers (corresponding to horizontal scales of around 3000 km), the *f*-mode displays strengthening about two days prior to AR formation and thus provides a new precursor for AR formation. Furthermore, we study two ARs, 12051 and 11678, apart from a magnetically quiet patch lying next to AR 12529, to demonstrate the challenges in extracting such a precursor signal when a newly forming AR emerges in a patch that lies in close proximity of one or several already existing ARs which are expected to pollute neighboring patches. We then discuss plausible procedures for extracting precursor signals from regions with crowded environments. The idea that the *f*-mode is perturbed days before any visible magnetic activity occurs at the surface can be important in constraining dynamo models aimed at understanding the global magnetic activity of the Sun.

*Subject headings:* Sun: dynamo — Sun: helioseismology — Sun: surface magnetism — turbulence

### 1. INTRODUCTION

Recent work has demonstrated the potential usefulness of employing the surface or fundamental *f*-mode in local helioseismology for detecting subsurface solar magnetism (Hanasoge et al. 2008; Daifallah et al. 2011; Felipe et al. 2012, 2013). While turbulence generally tends to lower the *f*-mode frequency (Fernandes et al. 1992; Murawski & Roberts 1993a; Duvall et al. 1998) relative to its theoretical value given by  $\omega_f = \sqrt{gk}$ , where  $g$  is the gravitational acceleration and  $k$  is the horizontal wavenumber, horizontal magnetic fields can increase the frequency (Murawski & Roberts 1993b), while vertical or inclined fields lead to a nonuniform behavior, depending on the value of the horizontal wavenumber (Singh et al. 2015). More importantly, however, horizontal *variability* of the subsurface magnetic field leads to a fanning of the *f*-mode, where changes in the integrated mode amplitude and position give clues about the depth of such a field (Singh et al. 2014). While these investigations demonstrated a number of previously unknown effects of the *f*-mode, they were restricted to idealizing conditions of an isothermal layer. In this Letter, we use observations with the Helioseismic and Magnetic Imager (HMI) on board the *Solar Dynamics Observatory* (*SDO*) to search for possible similarities between observations and simulations.

We focus on the possibility of using changes in the *f*-mode to predict the emergence of active regions (ARs) days before they can be seen in magnetograms. Owing to

the very nature of the *f*-mode being confined to the proximity of the surface, our approach is most sensitive to magnetic fields at shallow depths of just a few megameters (Mm), and ceases to be sensitive when the AR begins to become fully developed. Earlier attempts of predicting the emergence of ARs employed time-distance seismology using *p*-modes and have suggested the occurrence of perturbations at larger depths of 40–75 Mm (Ilonidis et al. 2011; Kholikov 2013). On the other hand, the rising flux tube scenario suggests a retrograde flow at a depth of 30 Mm (Birch et al. 2010), which has not been observed (Birch et al. 2016). Also morphological studies in the case of AR 11313 have suggested incompatibilities with the rising flux tube model (Getling et al. 2016). By contrast, in the distributed dynamo scenario (Brandenburg 2005), magnetic flux concentrations form spontaneously near the surface (Brandenburg et al. 2011, 2013), which might explain the aforementioned field concentrations at shallow depths. Spontaneous surface flux concentrations have also been seen in the deep hydromagnetic convection simulations of Stein & Nordlund (2012), where an unstructured magnetic field is allowed to enter the bottom of their computational domain. Such near-surface magnetic concentrations are expected to affect the *f*-mode as its eigenfunction peaks only a few Mm below the solar surface (cf. Schou 1999). It is possible that these perturbations could manifest themselves through detectable signatures.

Readers familiar with the conventional picture of buoyant flux tube emergence (as reviewed by, e.g., Charbonneau 2010) might be concerned about depths

as shallow as just a few Mm, because buoyant tubes of several kilogauss would reach the surface within an hour ( $\sim 3$  hours from the depth of 7.5 Mm in the simulations of Cheung et al. 2010), but this picture ignores the formation process and implants flux tubes as alien objects within the turbulent convection zone. By contrast, ARs and sunspots might instead be generated by the subsurface turbulence in ways similar to what has so far only been seen in idealized simulations (Brandenburg et al. 2013; Warnecke et al. 2013; Mitra et al. 2014). The point here is not to defend this idea, but to raise awareness of alternative viewpoints that would facilitate the understanding of the results presented below in the present work.

Once the AR has been detected in magnetograms and becomes fully developed, the  $f$ -mode amplitude begins to be suppressed. This might be explained by the fact that the interaction of both  $f$ - and  $p$ -modes with ARs or sunspots leads to mode conversion, resulting in the absorption of mode power (Thomas, et al. 1982; Cally et al. 1994; Cally & Bogdan 1997). This would explain the observed reduction of the mode amplitude *after* the analyzed AR has been formed. However, what was not discussed earlier is that the mode amplitude from the same region can undergo a *transient* growth phase prior to the actual flux emergence. This results in a nonmonotonic temporal variation in the normalized mode power which first rises, reaches a maximum value a few days before there is any sign of flux emergence, and then decreases as the strength of the magnetic field in that region increases. Although a proper explanation of this is not yet available, one might speculate that this could also be due to some kind of scattering, whereby  $p$ -modes would scatter off the magnetic flux concentrations and leak into enhanced  $f$ -mode power.

## 2. DATA ANALYSIS

We use line-of-sight (LoS) Dopplergrams and magnetograms from observations with HMI, mostly in the cylindrical equal-area projection mappings that are publicly available on the Joint Science Operations Center at Stanford<sup>1</sup>. Our analysis is based on 45 seconds cadence data with a projection scale of  $0.03^\circ$  per pixel, where the data represent the LoS Doppler velocity  $v(x, y, t)$  as a function of horizontal position  $(x, y)$  and time  $t$ . For each of the regions of interest, we consider a patch of  $512^2$  pixels covering an area of about  $(180 \text{ Mm})^2 \approx (15^\circ)^2$  on the solar surface. We track these patches for several days using a frame of reference corotating with the mean (Carrington) rotation rate  $\Omega_0$  with  $\Omega_0/2\pi = 424 \text{ nHz}$ . To capture transient signatures, we use data cubes  $v(x, y, t)$  of only 8 hours duration for the entire tracking period of our target region. To reduce the noise level arising from solar convection (Zhao et al. 2015) and effects from latitudinal differential rotation (J. Zhao, private communication), we use a running difference to the original images before storing  $v(x, y, t)$ .

We divide our five or six day stretches into 15 or 18 intervals of 8 hrs, each resulting in a data cube of  $512^2 \times 640$  points of  $v(x, y, t)$  that is Fourier transformed to give  $\hat{v}(k_x, k_y, \omega)$ , which too has the dimension  $\text{m s}^{-1}$  in our normalization. We then construct power spectra from

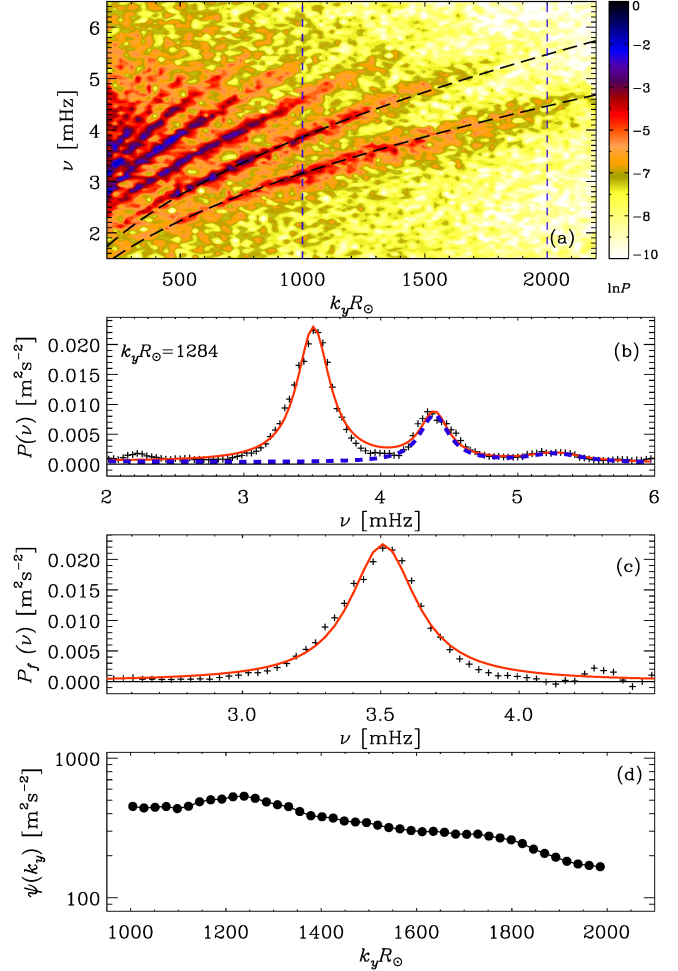


FIG. 1.— (a) Typical  $k\omega$  diagram where the lowest ridge is the  $f$ -mode, here for the quiet sun during 2010 May 14; (b) example of a vertical cut at a specified value of  $k_y R_\odot$  (plus symbols) together with the model fit (solid, red curve) and  $P_{\text{cp}}$  (dashed, blue line); (c)  $f$ -mode ridge ( $P_f$ , plus symbols) and the corresponding fit (solid, red curve); (d)  $\psi(k_y)$  for the full range enclosed within the vertical dashed lines in (a).

$P = |\hat{v}|^2$  and select  $k_x = 0$  in the subsequent analysis. Thus, we ignore longitudinal variations that could be affected by the cylindrical equal-area projection, as the latitudinal directions are expected to be the least sensitive to artifacts resulting from projection and also differential rotation. Also, our target regions were chosen such that the patches were always far from the limb during the entire tracking period. The thus obtained power spectra  $P(k_x = 0, k_y, \omega)$  are then used to construct a diagnostic  $k\omega$  diagram in the  $k_y - \omega$  plane; see Figure 1(a) which displays the  $f$ - and  $p$ -ridges where the horizontal wavenumber is  $k = k_y$ .

We now take a cut parallel to the frequency axis at a fixed  $k_y R_\odot$  to get the line profiles of the  $f$ - and lowest two  $p$ -ridges. We then apply boxcar smoothing along the frequency axis with a box width of 0.24 mHz. To determine the strength of the  $f$ -mode, we remove first the continuum and the lowest two  $p$ -ridges, which are represented by a superposition of parabolic and Lorentzian fits, respectively and denoted by  $P_{\text{cp}} = |\hat{v}|_{\text{cp}}^2$ , where the subscript cp stands for the sum of continuum and  $p$

<sup>1</sup> <http://jsoc.stanford.edu/>

modes; see Figures 1(b) and (c). In most cases we repeat the same procedure at all wavenumbers in the range  $k_y R_\odot \in [1200, 2000]$ , and determine the  $f$ -mode power as  $P_f(k_y, \omega) = |\hat{v}_f|^2 = P - P_{\text{cp}}$ . We may define the integrated  $f$ -mode amplitude assuming circularly symmetric rings in the  $k_x$ - $k_y$  plane as

$$\langle v^2 \rangle_f = 2AT \int_0^\infty \int_0^\infty k P_f(k, \omega) \frac{dk}{2\pi} \frac{d\omega}{2\pi}, \quad (1)$$

where  $k^2 = k_x^2 + k_y^2$ , and write  $\langle v^2 \rangle_f$  as

$$\langle v^2 \rangle_f = L \sum_k k P_{f,k} \text{ with } P_{f,k} = 2 \sum_\omega P_f(k, \omega), \quad (2)$$

where  $A = L^2$  is the area of the chosen patch,  $L$  is the side length and  $T$  is the tracking time of the data cube. Thus, we can determine the energy of the  $f$ -mode,  $E_f$ , characterizing its strength, as:

$$E_f(t) \equiv \frac{1}{2} \langle v^2 \rangle_f(t) = \frac{1}{2} \left( \frac{L}{R_\odot} \right) \sum_k \psi(k) \quad (3)$$

with  $\psi(k) = k R_\odot P_{f,k}$ ; see Figure 1(d). Note that we determine the above quantities by setting  $k_x = 0$  and choosing a high-wavenumber range,  $k_y R_\odot \in [1200, 2000]$ , unless otherwise specified. Although this choice of considering only high wavenumbers in assessing the strength of the mode is not a standard procedure, we nevertheless focus on this regime as this “precursor signal” appears to be localized at such large wavenumbers; see Section 4 below. The time dependence of  $E_f$  may now be determined by computing the above quantities from the sequence of 8 h data cubes prepared for all tracked regions of interests.

Even in the quiet phase during solar minimum,  $E_f$  shows a systematic dependence on the angular distance  $\alpha$  from the disk center, given by

$$\cos \alpha = \cos \vartheta \cos \varphi; \quad \varphi = \varphi_* - \varphi_0 + \Omega_{\text{syn}} t, \quad (4)$$

with  $\vartheta$  and  $\varphi$  being respectively the latitude and longitude of the point of interest,  $\varphi_*$  is the corresponding Carrington longitude,  $\varphi_0$  is the Carrington longitude of the disk center at the time when we began tracking the target patch, and  $\Omega_{\text{syn}} = 2\pi/27.275$  days is the mean synodic Carrington rotation rate of the Sun (i.e., the apparent rotation rate as viewed from the Earth).

As suggested by earlier work (Singh et al. 2014), we focus on  $E_f$  for fairly large  $k_y$ . We track a particular position on the solar surface in time using the average (Carrington) rotation rate. Normalizing by the solar radius  $R_\odot = 700$  Mm gives the spherical harmonic degree  $k_y R_\odot$ . For a fixed range of  $k_y R_\odot$ , we compute the dependence of  $E_f$  on  $t$ . Empirically, the value of  $E_f$  for the quiet sun (the position where no AR emerges within the next few days) shows a systematic variation that is approximately of the form

$$\zeta(\cos \alpha) = \cos \alpha [q + (1 - q) \cos \alpha] \text{ with } q = 0.5. \quad (5)$$

This function obeys  $\zeta = 1$  at  $\alpha = 0$  (disk center). It is then useful to define

$$\tilde{E}_f \equiv E_f / \zeta, \quad (6)$$

which fluctuates moderately about some average value in the quiet phase of the Sun. However, several days *prior* to the emergence of an AR, our studies show elevated values of  $\tilde{E}_f$  at that corotating patch where this AR later emerges.

It would be interesting to see whether there are other indicators, for example in the magnetic field itself, which could also give early indications of AR formation. Magnetic properties from regions of interest on the solar disk might offer insight into the process of developing ARs. The LoS magnetic field ( $B$ ) varies randomly in space and time, and has a narrow distribution with positive and negative polarities nearly balancing themselves out when the localized patch is magnetically quiet. Let us denote by  $f_B$  the normalized probability distribution function (PDF) of  $B$  in a chosen patch at any given time, such that

$$\int_{-\infty}^\infty f_B dB = 1. \quad (7)$$

The kurtosis, kurt  $B$ , of the distribution  $f_B$  is defined as,

$$\text{kurt } B = \frac{1}{\sigma_B^4} \int_{-\infty}^\infty (B - \bar{B})^4 f_B dB, \quad (8)$$

where the mean ( $\bar{B}$ ) and the variance ( $\sigma_B$ ) of  $f_B$  are

$$\bar{B} = \int_{-\infty}^\infty B f_B dB \text{ and } \sigma_B^2 = \int_{-\infty}^\infty (B - \bar{B})^2 f_B dB, \quad (9)$$

respectively. For a normal distribution, kurt  $B = 3$ , while excess kurtosis, kurt  $B \gg 3$ , indicates a heavy-tailed distribution. We monitor the temporal evolution of kurt  $B$  from the localized patches that we track on the solar disk as the Sun rotates.

It is useful to make a simultaneous comparison with the value for relatively quiet patches under otherwise identical local conditions. This may be realized as follows: corresponding to each target region at  $(\vartheta, \varphi)$ , we consider a (quiet) mirror region at  $(\vartheta^\dagger, \varphi)$  in the opposite hemisphere with the same dimensions, and track both these patches simultaneously, where  $\vartheta^\dagger = -\vartheta$  for the entire tracking period. We refer to the  $f$ -mode energy from such a mirror region as  $E_f^\dagger$ . We find that, while the rms magnetic field  $B_{\text{rms}}$  rises when the AR emerges, the value in the mirror region,  $B_{\text{rms}}^\dagger$ , remains close to a constant background value.

### 3. SAMPLE SELECTION

We have selected a number of ARs, which may be broadly classified under the following two categories:

- *Isolated ARs:* In these examples, ideally a single AR emerges in isolation, with the rest of the Sun being nearly magnetically quiet. As the seismic signals may well be nonlocal, we first need to study isolated ARs to assess the  $f$ -mode perturbation due to subsurface magnetic fields associated with newly developing ARs. This would allow us to avoid contamination that might be caused by the presence of already existing ARs in the neighborhood of the patch where a new AR is going to form later. There are not many instances since the launch of *SDO*, where only a single AR appears on the entire solar disk, and therefore we have included a

few more cases wherein the other ARs are at least far ( $> 300$  Mm) from the AR in emergence. The chosen examples in this class include ARs 11130, 11158, 11242, 11105, 11072 and 11768.

- *Crowded ARs:* It would be a serious limitation if the proposed technique applies only to isolated ARs, and therefore we have also studied the effects of a newly forming AR on a patch that lies in close proximity to one or several already existing ARs. To highlight the challenges one might face in extracting the signal from such an AR, we have studied ARs 12051 and 11678.

Furthermore, in order to avoid systematic effects close to the limb, we have restricted our sample to only those cases which lie within  $\pm 60^\circ$  in both latitude and longitude of the disk center. Yet another requirement limiting our sample size is that the corresponding mirror patches in the opposite hemisphere must be magnetically quiet for the entire tracking period, thus offering an easy and simultaneous control.

We also studied four magnetically quiet patches at two different phases of the solar magnetic activity cycle. Two such patches, symmetrically located in the northern and the southern hemispheres, were chosen when the Sun was just coming out of its minimum during 2010 May. This offers another control when the Sun did not show much magnetic activity for a few days. We then chose a magnetically quiet patch lying next to AR 12529 during 2016 April, and also followed simultaneously its mirror counterpart.

## 4. RESULTS

### 4.1. Isolated ARs

In Figures 2 and 3 we compare the quiet sun during 2010 May 14–19 with an active sun during 2010 November 26–30. We show the time traces of  $\tilde{E}_f$  for corotating patches. In Figure 2,  $t_{\text{CM}}$  denotes the time of central meridian crossing while in Figure 3,  $t_{\text{AR}}$  is the time at which later the AR emerges. We compare with the time traces of the mirror region  $\tilde{E}_f^\dagger$  in panels (a) of those and subsequent figures, kurt  $B$  from those patches in panels (b), the rms magnetic field  $B_{\text{rms}}$  within those patches in panels (c), as well as the corresponding full disk LoS magnetograms either at  $t = t_{\text{AR}} - 2\text{d}$  or at  $t = t_{\text{AR}} - 1\text{d}$  in panels (d) and at  $t = t_{\text{AR}}$  in panels (e), which are the times when the ARs emerge and were assigned their numbers. The dash-dotted (red) and triple-dot-dashed (orange) lines in panels (c) denote respectively the time-traces of  $0.08 B_{\text{max}}$  and  $-0.08 B_{\text{min}}$  from the patch of interest where an AR develops. All six ARs show similar characteristics: an early rise of  $\tilde{E}_f$  with a maximum 1–2 days prior to  $t_{\text{AR}}$ , followed by a decline at and after  $t_{\text{AR}}$ , as well as a delayed increase of  $\tilde{E}_f^\dagger$ , sometimes with a maximum near  $t_{\text{AR}}$ . We speculate that the delayed increase of  $\tilde{E}_f^\dagger$  might be caused by a correlated response at a distant mirror patch. This would indicate that the early  $f$ -mode strengthening, i.e., the precursor signal, appears to have an associated causal response at later times, at distant mirror patches. Interestingly enough, in most cases, the kurt  $B$  from the patch where an AR

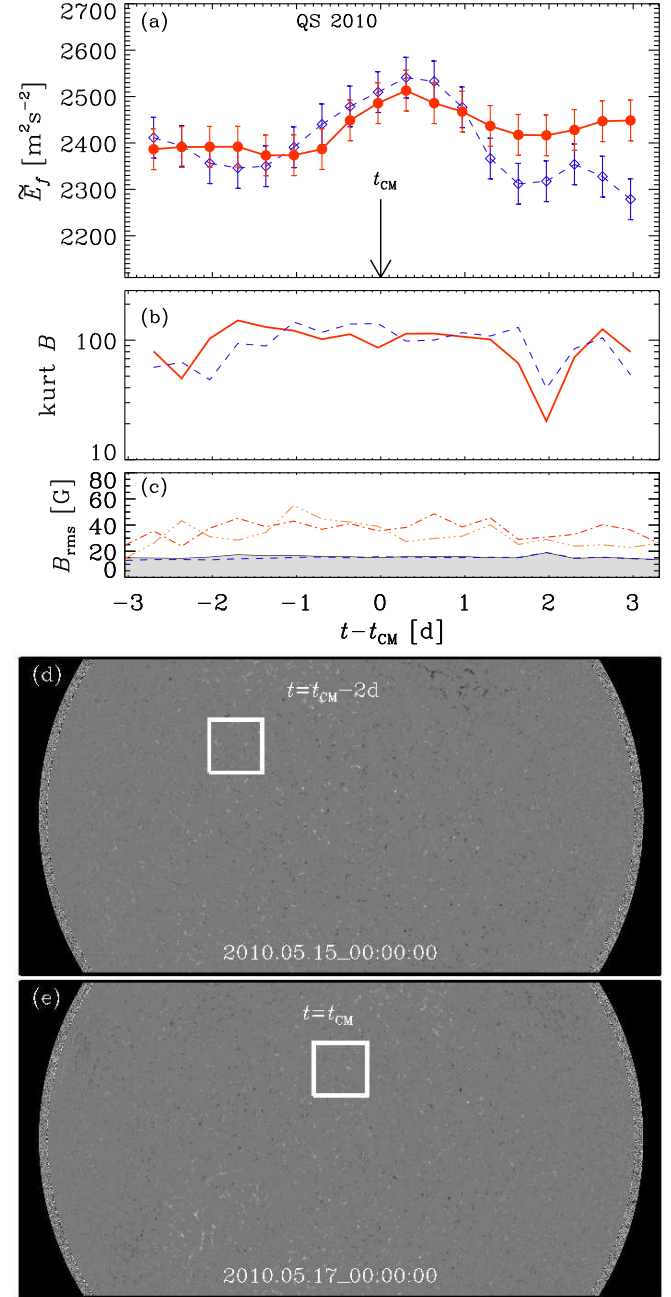


FIG. 2.— Time traces of  $\tilde{E}_f$  (solid red;  $\vartheta = +20^\circ$ ) and  $\tilde{E}_f^\dagger$  (dashed blue;  $\vartheta = -20^\circ$ ) as a function of  $t - t_{\text{CM}}$  in panel (a), evolutions of the kurtosis, kurt  $B$  (solid red) and kurt  $B^\dagger$  (dashed blue) in panel (b),  $B_{\text{rms}}$  (solid line with shaded area underneath) together with  $B_{\text{rms}}^\dagger$  (dashed blue line) in panel (c), as well as magnetograms at  $t = t_{\text{CM}} - 2\text{d}$  (d) and  $t = t_{\text{CM}}$  (e) for the quiet sun during 2010 May 14–19. The dash-dotted (red) and triple-dot-dashed (orange) lines denote the time-traces of  $0.08 B_{\text{max}}$  and  $-0.08 B_{\text{min}}$ , respectively from the patch in the northern hemisphere.

forms also shows a peak before the AR is fully developed, and thus offers yet another advance indication of AR formation.

By contrast, during a suitably chosen time in 2010, the Sun was nearly completely quiet, and both  $\tilde{E}_f$  and  $\tilde{E}_f^\dagger$  follow each other rather closely (Figure 2), although their time traces still show considerable variability. This might

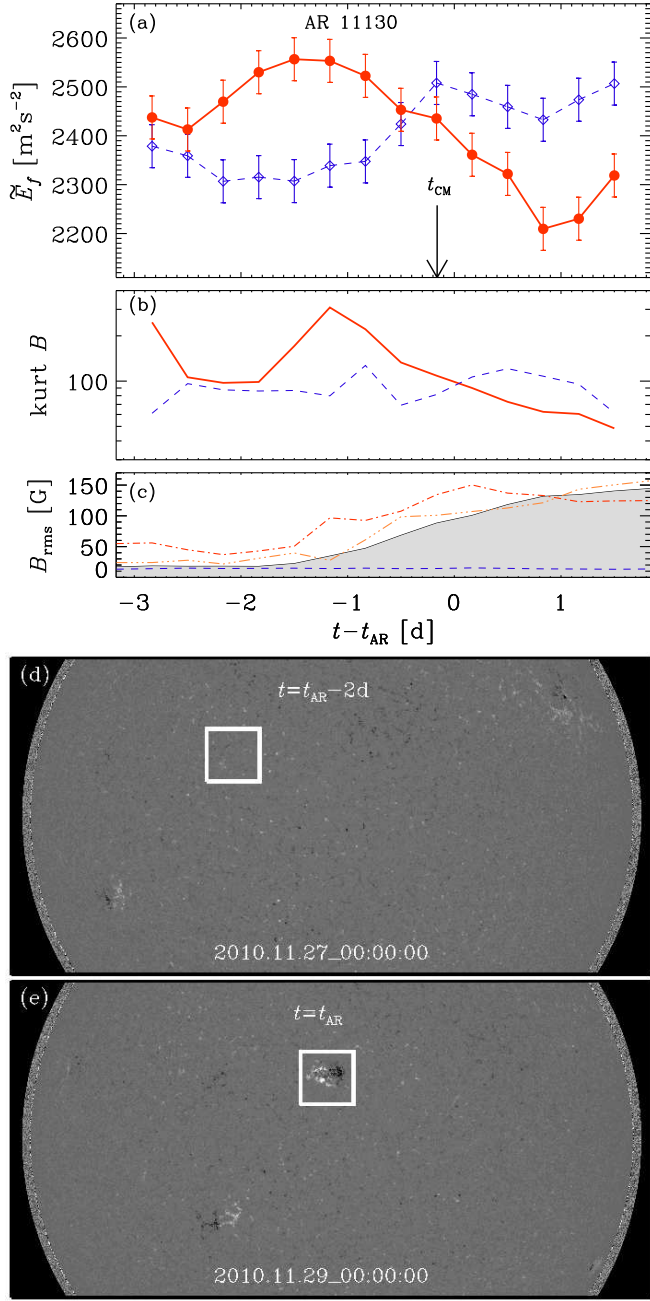


FIG. 3.— Time traces of  $\tilde{E}_f$  (solid red line) and  $\tilde{E}_f^\dagger$  (dashed blue line) as a function of  $t - t_{\text{AR}}$ , with  $t_{\text{CM}}$  marking the time of central meridian crossing in panel (a), evolutions of the excess kurtosis,  $\gamma_B$  (solid red) and  $\gamma_B^\dagger$  (dashed blue) in panel (b),  $B_{\text{rms}}$  (solid line with shaded area underneath) together with  $B_{\text{rms}}^\dagger$  (dashed blue line) as a function of  $t - t_{\text{AR}}$  (c), as well as magnetograms at  $t = t_{\text{AR}} - 2\text{d}$  (d) and  $t = t_{\text{AR}}$  (e) for AR 11130. The dash-dotted (red) and triple-dot-dashed (orange) lines denote the time-traces of  $0.08 B_{\text{max}}$  and  $-0.08 B_{\text{min}}$ , respectively from the patch where the AR 11130 develops.

be caused by fluctuations in the subsurface turbulence and small-scale magnetic fields even for the quiet sun, or perhaps by instrumental effects. The fact that  $\tilde{E}_f$  and  $\tilde{E}_f^\dagger$  remain close to each other at all times shows that in the quiet phase of the Sun, the integrated  $f$ -mode amplitudes in the two hemispheres evolve *symmetrically*, so that the

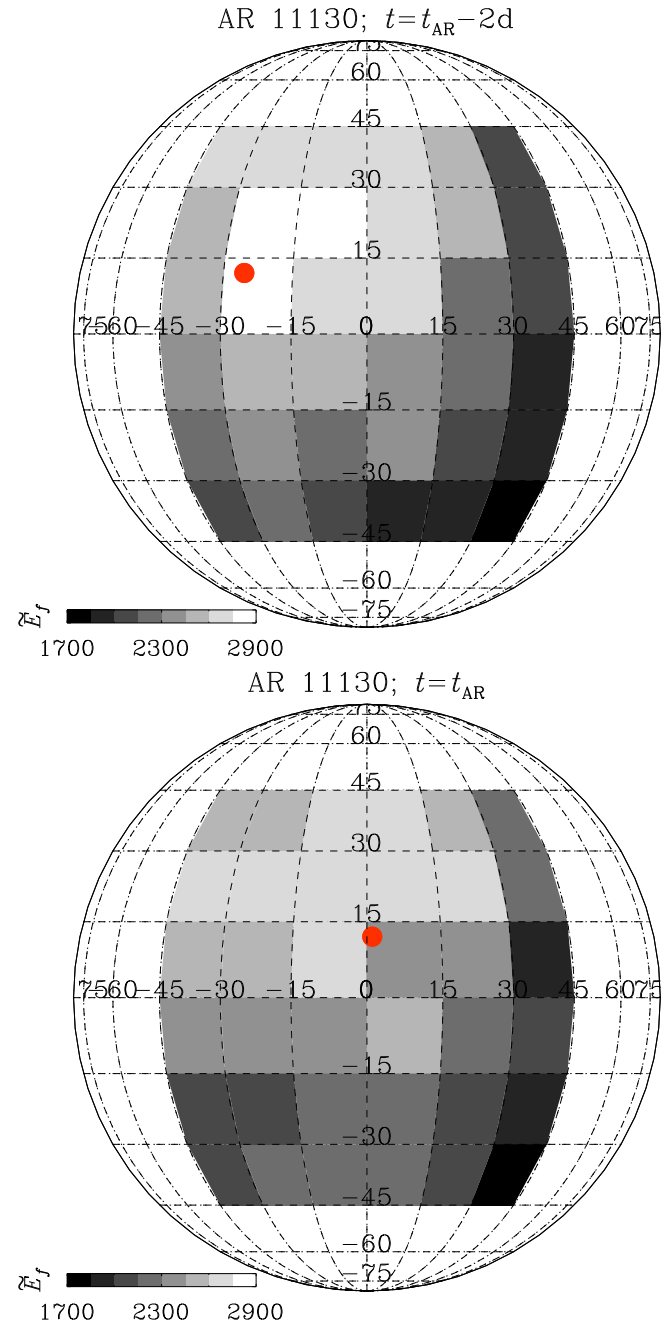


FIG. 4.— Images of  $\tilde{E}_f$  for a relatively quiet phase of the Sun in 2010 when an isolated AR 11130 emerged on 2010 November 29. Top and bottom panels show images of  $\tilde{E}_f$  two days before the AR emergence and at  $t = t_{\text{AR}}$ , respectively. Red filled circle denotes the location of AR 11130. Postel projection mapping was used in constructing these images.

difference is small and therefore not significant. Note also that, since no AR has emerged during that time, we replaced  $t_{\text{AR}}$  by the time of central meridian crossing  $t_{\text{CM}}$  of an arbitrarily chosen comoving patch in Figure 2.

Based on these findings, the following hypotheses may be formulated. In regions with low or no surface magnetic activity, a nearly flat time trace without systematic differences between  $\tilde{E}_f$  and  $\tilde{E}_f^\dagger$  suggests low subsurface magnetic activity, while a gradual and systematic en-

hancement of  $\tilde{E}_f$  relative to  $\tilde{E}_f^\dagger$  is suggestive of a build-up of subsurface magnetic activity. In already established ARs, on the other hand,  $\tilde{E}_f$  is visibly depressed and  $\tilde{E}_f^\dagger$  may or may not show a marked rise, depending on the complexity of the already established surface activity.

We adopt a root-mean-square error estimation for  $\tilde{E}_f$  based on the results shown in Figure 2 for a magnetically quiet sun. The mean error ( $\sigma_m$ ) is obtained from:

$$\sigma_m = \frac{1}{2} \sqrt{\sigma_E^2 + \sigma_{E^\dagger}^2}; \sigma_E = \sqrt{\left\langle \left( \tilde{E}_f - \bar{\tilde{E}}_f \right)^2 \right\rangle}. \quad (10)$$

Here,  $\langle \tilde{E}_f \rangle \equiv \bar{\tilde{E}}_f$  denotes the mean value of  $\tilde{E}_f(t)$ . We use  $\sigma_m$  to display error bars in figures showing  $\tilde{E}_f(t)$ .

Let us now discuss the individual examples in more detail. AR 11130 was a solitary AR during 2010 when the overall solar activity was still rather low. It is therefore an example where interference from other locations on the Sun is minimal. Indeed, it displays most strikingly the “symmetry breaking” between  $\tilde{E}_f$  and  $\tilde{E}_f^\dagger$ , with  $\tilde{E}_f$  showing a maximum about 1.5 days before this AR emerges; see Figure 3. Also,  $\text{kurt } B$  shows a peak more than one day before this AR is fully developed; see the solid red line in Figure 3(b).

As an extension of this work, we also calculate images of  $\tilde{E}_f$  for the solar disk. This gives more explicit information of where the next AR might form; see Figure 4 showing images at times when AR 11130 was forming. It is remarkable that the maximum in  $\tilde{E}_f$  at time  $t = t_{\text{AR}} - 2d$  coincides with the location (marked by a red filled circle) where AR 11130 is going to form later. We also note from the top image in Figure 4 that the strengthening of the  $f$ -mode about two days prior to the emergence of the AR is nonlocal in space, with patches progressively farther from the predicted location of AR 11130 showing almost monotonically decreasing  $\tilde{E}_f$ . Although we see a moderate degree of fluctuation, there are also systematic effects—especially near the limb. Whether or not these are caused by instrumental effects such as variations of the modulation transfer function (Wachter et al. 2012) is unclear. If so, the remaining variations may either also be related to instrumental effects or they could be caused by weaker subsurface magnetic fields that must always be present—even during solar minimum.

Next, we consider AR 11158 (Figure 5), which was a rapidly growing AR that produced the first X-class flare of solar cycle 24 on 2011 February 15 (Maurya et al. 2012) with an Earth-directed halo coronal mass ejection (Schrijver et al. 2011). It also produced several M-class flares during February 13–16 (Inoue et al. 2013), after being assigned its number on February 13. Also in this case,  $\tilde{E}_f$  shows a clear increase with  $\tilde{E}_f - \tilde{E}_f^\dagger \sim 200 \text{ m}^2 \text{s}^{-2}$  about a day before  $B_{\text{rms}}$  reaches a plateau of about 220 G. The energy increase of about  $\sim 300 \text{ m}^2 \text{s}^{-2}$  seen about three days prior to the AR emergence appears to be indicative of a subsurface concentration of the magnetic field resulting in a rapid growth of  $B_{\text{rms}}$  in the photosphere. Thus, the same general trend is found here too, although the potential for using  $\tilde{E}_f(t)$  as a precursor was less clear in the sense that it showed a maximum

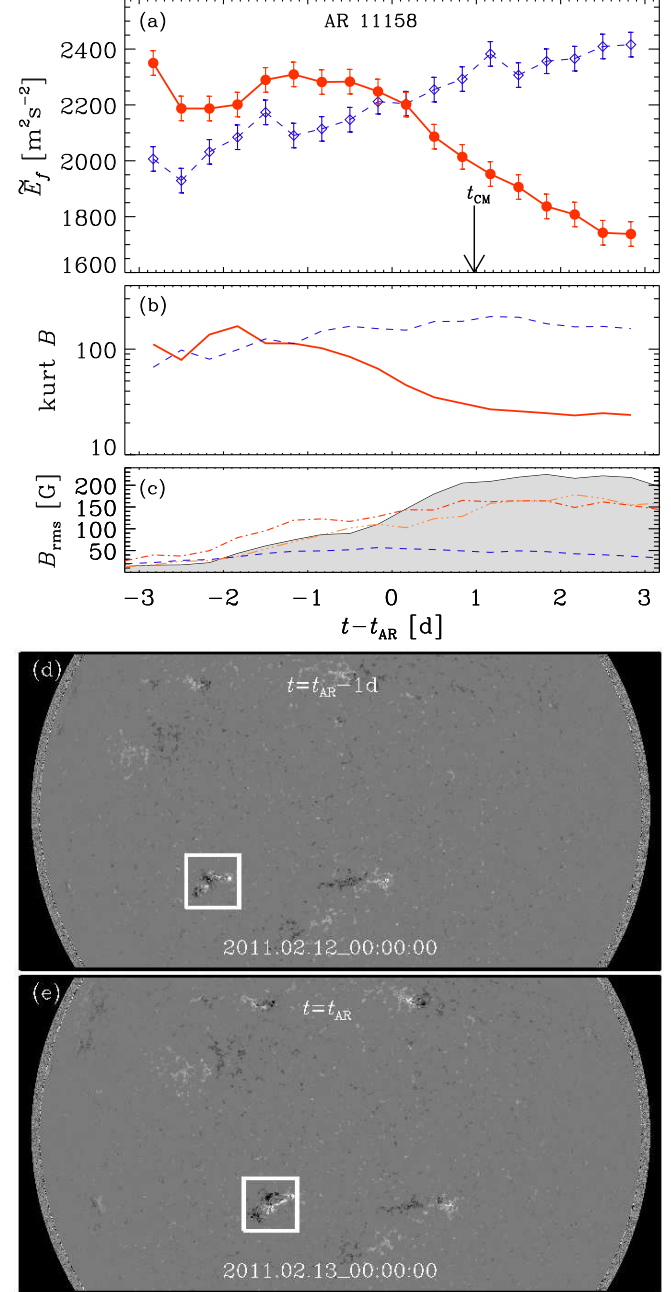


FIG. 5.— Same as Figure 3, but for AR 11158.

only about a day in advance. The subsequent increase in  $\tilde{E}_f^\dagger$  is noticeable here as well. In this case,  $\text{kurt } B$  shows a peak already at  $t = t_{\text{AR}} - 2d$ .

AR 11242 (Figure 6) was assigned its NOAA number on 2011 June 29, a day before it fully emerged in isolation. Here we find elevated values of  $\tilde{E}_f$  relative to  $\tilde{E}_f^\dagger$  for all times during our tracking period, where  $\tilde{E}_f$  shows a maximum about 1–2 days prior to AR formation. Again, early strengthening of  $\tilde{E}_f$  at  $t = t_{\text{AR}} - 3d$  appears as a precursor to the rise of  $B_{\text{max}}$  and the peak in  $\text{kurt } B$  at  $t = t_{\text{AR}} - 1d$ . In this case too, we have strong evidence of  $f$ -mode strengthening about 1–3 days before there is any

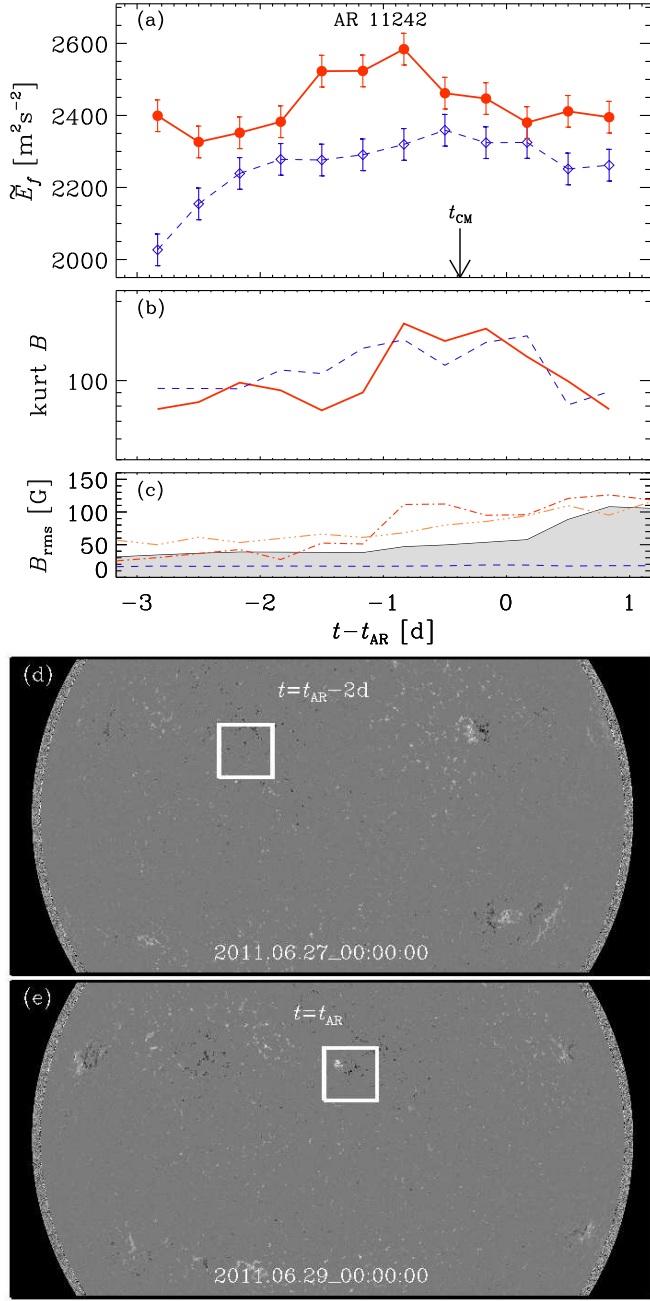


FIG. 6.— Same as Figure 3, but for AR 11242.

visible magnetic activity at the patch where AR 11242 develops later. Smirnova et al. (2013) reported long-period oscillations of 200–400 min associated with this AR, using simultaneous data from HMI and ground-based radio emission measurements at 37 GHz from Metsähovi radio observatory at Aalto University in Finland. They interpreted their results based on the shallow sunspot model of Solov'ev & Kirichek (2009), which may even show some resemblance to the magnetic flux concentrations that form spontaneously in strongly stratified turbulence simulations (Brandenburg et al. 2013).

Now we consider the case of AR 11105 (Figure 7), which was assigned its NOAA number nearly at the time of onset of  $B_{\text{rms}}$  on 2010 September 3. For AR 11105,

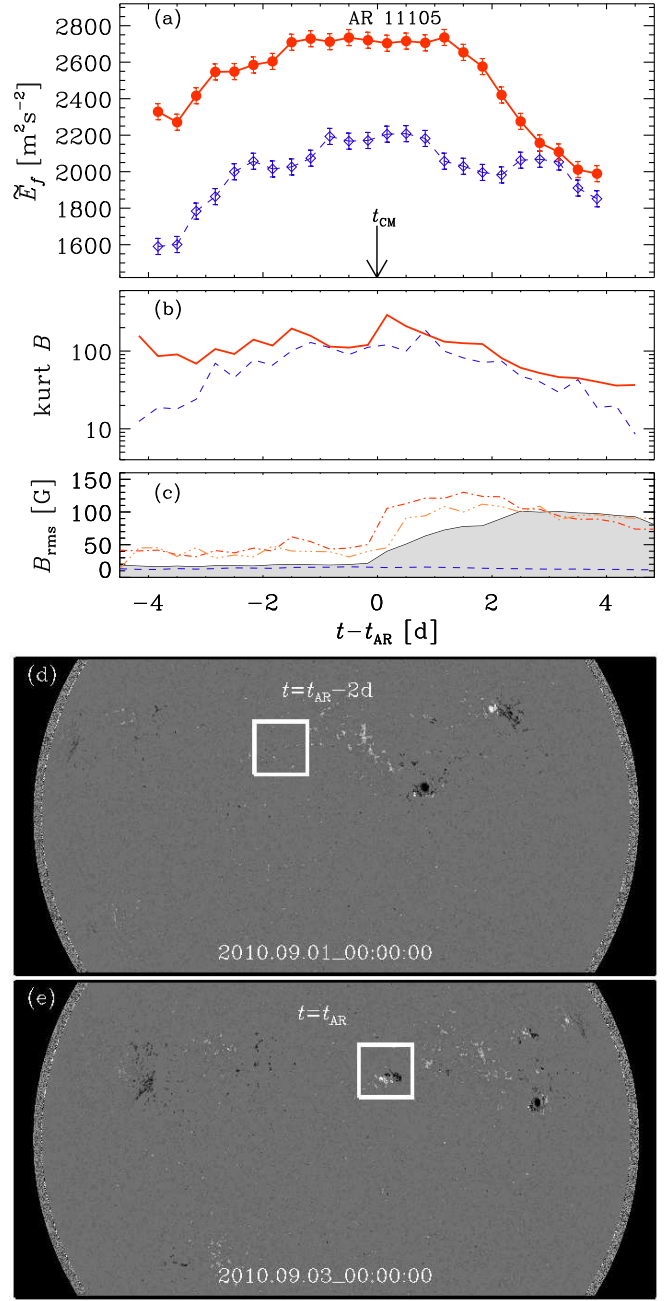


FIG. 7.— Same as Figure 3, but for AR 11105.

similar to the previous example,  $\tilde{E}_f$  remains larger than  $\tilde{E}_f^\dagger$  during the tracking, and shows the usual post-emergence damping. Unlike the other examples, the time trace of  $\text{kurt } B$  is in this case featureless.

Next we turn to AR 11072 (Figure 8), which was identified on 2010 May 23 when  $B_{\text{rms}}$  had reached its peak value, although  $B_{\text{max}}$  from the same region showed an early growth already about two days earlier. About four days prior to  $t_{\text{AR}}$ , the patch in this case was much closer to the limb than in the other examples and the data might have suffered some systematic effects, as discussed above. However, we do find weak signatures of relative strengthening of  $\tilde{E}_f$  at  $t \approx t_{\text{AR}} - 3.5\text{d}$ , although the

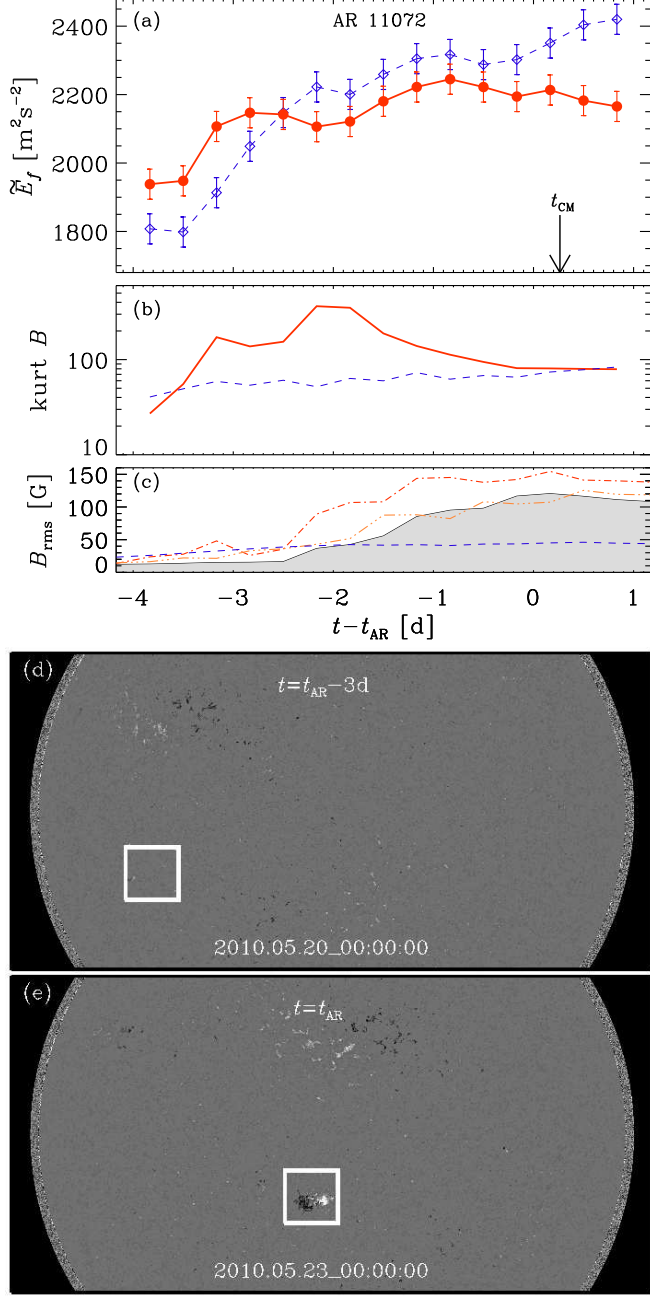


FIG. 8.— Same as Figure 3, but for AR 11072.

damping of the  $f$ -mode after the flux emergence is not seen. This might be due to the episodic flux emergences in this case, as is apparent from Figure 8. Interestingly,  $\text{kurt } B$  shows a sharp rise at about the same time when we find signs of  $f$ -mode strengthening, and it exhibits a double-peaked feature, which is all much before  $B_{\text{rms}}$  saturates in this region.

For AR 11768, we now perform the following experiment to highlight the significance of wavenumber dependence of the proposed precursor signal, i.e., the  $f$ -mode strengthening, and have presented our results for this case in Figures 9 and 10. We considered two different wavenumber intervals in determining  $E_f$  using Equation (3); while Figure 9(a) corresponds to the same range,

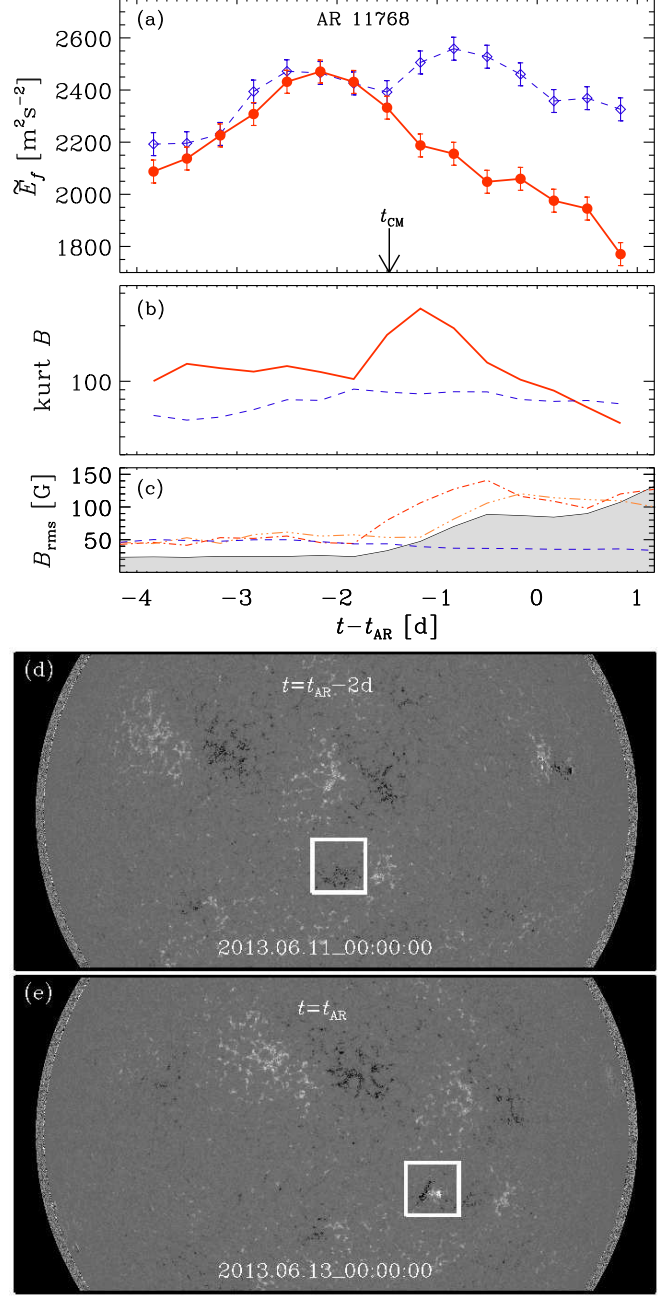


FIG. 9.— Similar to Figure 3, but for AR 11768.

$k_y R_\odot \in [1200, 2000]$ , as used in the other cases, for Figure 10 we chose a much narrower wavenumber range,  $k_y R_\odot \in [1200, 1300]$ , which explains the lower values of  $\tilde{E}_f$ . As shown in Figure 10, there is again the characteristic symmetry breaking between  $\tilde{E}_f$  and  $\tilde{E}_f^\dagger$ , with  $\tilde{E}_f$  showing a maximum at  $t = t_{\text{AR}} - 2\text{d}$ . In this case the initial rise is sharper than, say, for AR 11130. However, no such relative strengthening of  $\tilde{E}_f$  is seen before emergence when the larger wavenumber range is considered, although the usual rise of  $\tilde{E}_f$  followed by the post-emergence damping is clearly visible; see Figure 9(a). This provides a hint of a possible wavenumber dependence of the effect causing the  $f$ -mode strengthen-

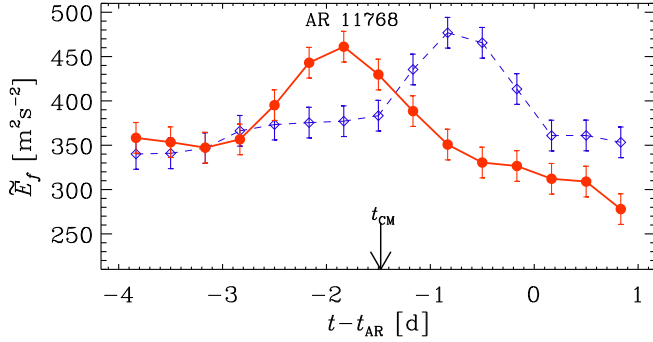


FIG. 10.— Similar to Figure 9(a), but using  $k_y R_\odot \in [1200, 1300]$  instead of  $[1200, 2000]$  in determining  $E_f$  using Equation (3).

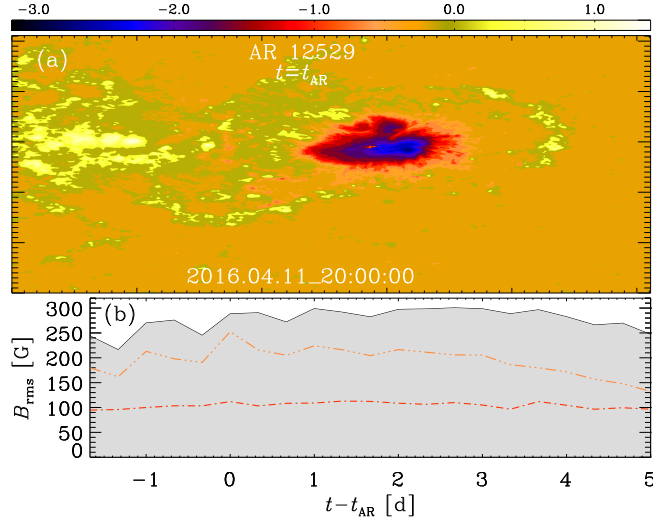


FIG. 11.— Panel (a) shows the AR 12529 with colors indicating the strength of the LoS magnetic field  $B$  in kG; panel (b) shows temporal evolution of its rms strength  $B_{\text{rms}}$  (solid line with shaded area underneath) together with  $B_{\text{rms}}^\dagger$  (dashed blue line). The dash-dotted (red) and triple-dot-dashed (orange) lines denote time-traces of  $0.08 B_{\text{max}}$  and  $-0.08 B_{\text{min}}$ , respectively from the patch shown in panel (a).

ing prior to AR formation. The perturbed wavenumbers of the  $f$ -mode correspond to horizontal scales of around 3000 km and we speculate that these might be the typical scales of magnetic structures that are gradually growing in both strength and size while retaining their imprints in terms of causing the observed  $f$ -mode strengthening correspondingly at such high wavenumbers. Note that in this case, large-scale patches of weak magnetic fields are present in the opposite hemisphere, with  $B_{\text{rms}}^\dagger \approx 2B_{\text{rms}}$  at early times, being highest of all the other cases. This could affect the values of  $\tilde{E}_f^\dagger$ . Here too,  $\text{kurt } B$  shows a peak about a day before the magnetic flux associated with this AR is fully emerged.

Comparing now all the six ARs in our sample, we see that the three ARs that appeared in the north (ARs 11130, 11242, and 11105) had slightly larger values of  $\tilde{E}_f$  ( $2600\text{--}2800 \text{ m}^2 \text{s}^{-2}$ ) than the three in the south (ARs 11158, 11072, and 11768 with  $\tilde{E}_f = (2200\text{--}2400 \text{ m}^2 \text{s}^{-2})$ ). This is consistent with the strong north-south asymmetry of cycle 24 with stronger activity and

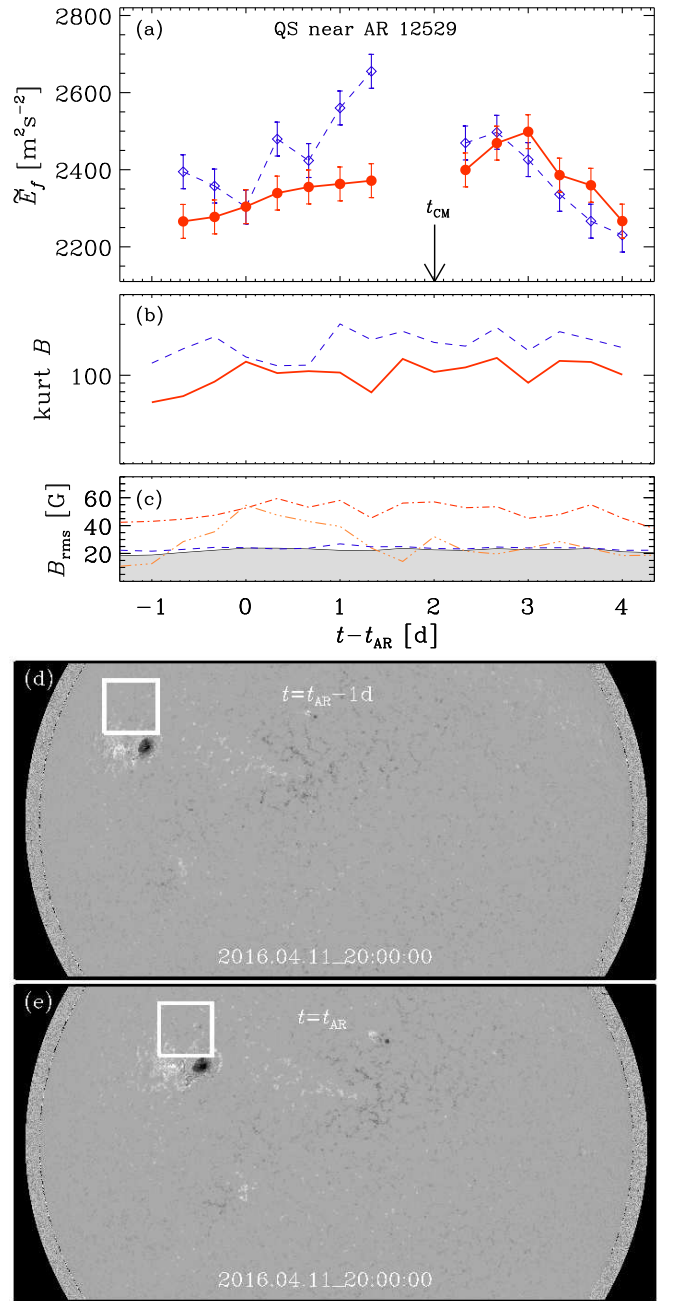


FIG. 12.— Similar to Figure 3, but for a magnetically quiet patch lying next to AR 12529. Here,  $t = t_{\text{AR}}$  corresponds to a maximum in  $|B_{\text{min}}|$ .

an earlier maximum in the north and weaker activity and a later maximum in the south (Chowdhury et al. 2013; Sun et al. 2015). This shows that the value of  $\tilde{E}_f$  reflects the general subsurface magnetic activity even over the time scale of the solar cycle.

#### 4.2. Crowded ARs

As argued above, the ARs cause damping of the  $f$ -mode after their emergence and this might influence the signal from a newly forming AR in the neighborhood. In order to extract precursor signals from a developing AR in a crowded environment, we perform an experiment demonstrating the nonlocality of the high-wavenumber

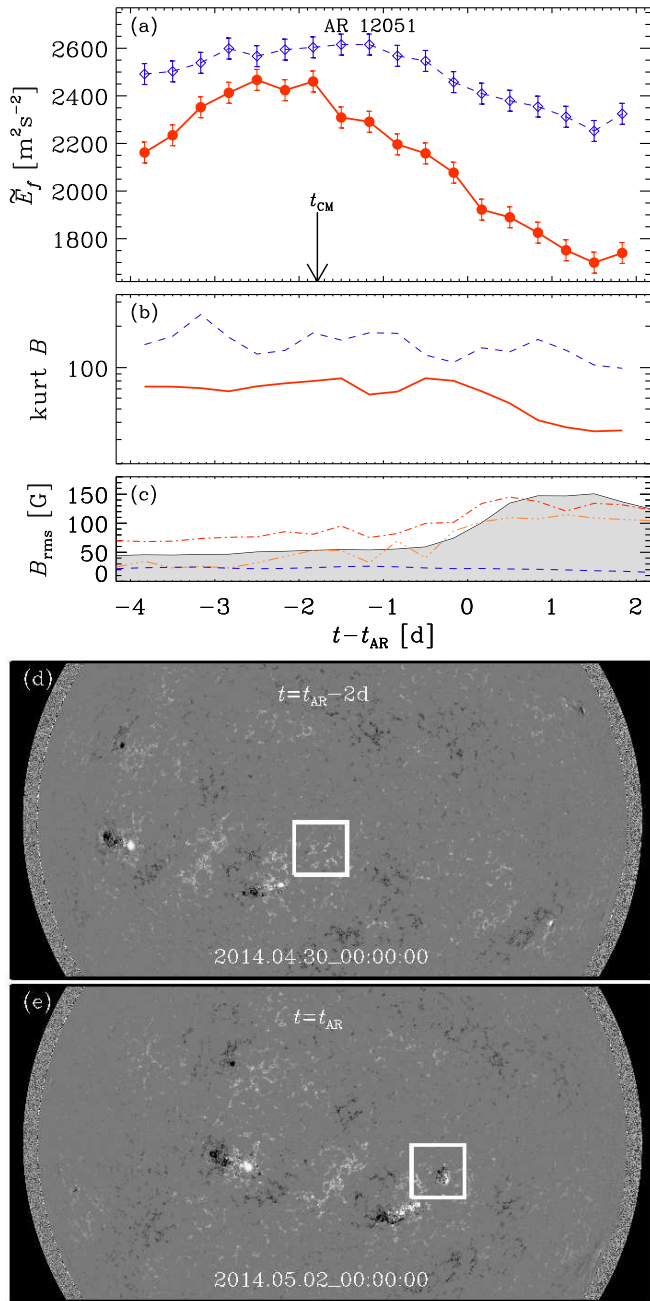


FIG. 13.— Same as Figure 3, but for AR 12051, which is in close proximity to already existing ARs.

*f*-mode damping caused by already established ARs. Here, we consider a magnetically quiet patch lying just above AR 12529, which was an already existing strong AR during 2016 April; see Figure 11(a), which shows a close-up of this AR and the temporal evolution of its  $B_{\text{rms}}$  in panel (b). Similar to, say, Figure 3, we show time traces of  $\tilde{E}_f$  (corresponding to the quiet patch above AR 12529) and  $\tilde{E}_f^\dagger$  in Figure 12. Note that both patches being tracked in this experiment are magnetically quiet and that their corresponding kurtoses are essentially featureless. We find a significant damping of  $\tilde{E}_f$  as compared to  $\tilde{E}_f^\dagger$  at  $t \approx t_{\text{AR}} + 1\text{d}$ , after which there are some

data gaps in the observations. Both  $\tilde{E}_f$  and  $\tilde{E}_f^\dagger$  attain similar values at late stages.

We now turn to the case of AR 12051, which lies next to bigger and stronger ARs that had appeared already in the southern hemisphere; see the magnetograms in panels (d) and (e) of Figure 13. Here too we find that the evolution of  $\tilde{E}_f$  obtained from the patch where later AR 12051 emerges is not flat; see Figure 13. It rises from a level of about  $\sim 2150 \text{ m}^2 \text{s}^{-2}$  and attains a maximum of  $\sim 2400 \text{ m}^2 \text{s}^{-2}$  more than two days before it was assigned its number on 2014 May 2 and nearly three days before  $B_{\text{rms}}$  reached its maximum value of about 150 G. On May 3, this AR developed a so-called  $\delta$ -class spot with M class flares a few days later. However, the essential difference here is that the  $\tilde{E}_f^\dagger$  from the relatively quiet mirror patch remains larger than  $\tilde{E}_f$  at all times. This might well be expected based on our experiments and results presented above and may be understood as follows: as the southern hemisphere is already “polluted” by many ARs, the *f*-mode is expected to be damped in this hemisphere and therefore the time-trace of  $\tilde{E}_f$  for AR 12051, while showing early precursor signatures, does not overcome  $\tilde{E}_f^\dagger$  from the northern hemisphere where the *f*-mode remains undamped and shows a much smaller variation.

Having discussed the possible difficulties in predicting a new AR emerging in a crowded environment, we now wish to describe plausible procedures that might be useful in still extracting the precursor signals in such “polluted” medium. One may be able to find guidance from a standard technique of optical astronomy where one routinely subtracts emission from a bright foreground star in order to detect and study a faint background source. In the present context, this would require a more detailed knowledge of the *f*-mode damping mechanism caused by existing ARs on the solar disk, so that one could apply a similar *cleaning* procedure. We make such an attempt for our final case of AR 11678, which emerged next to a group of compact ARs on 2013 February 19. In Figure 14 we show such a plot. Although the time-trace of  $\tilde{E}_f$  shows a peak about a day before this AR emerges, it remains smaller than  $\tilde{E}_f^\dagger$  at all times of tracking, as would be expected in this case. Based on the other cases discussed earlier, we find that the amount of observed damping of  $\tilde{E}_f$  could be as large as about 25% of its peak value. Therefore, we applied a uniform boost of 25% to the original  $\tilde{E}_f$  in an attempt to correct against the expected damping, and show the thus boosted time-trace of  $1.25\tilde{E}_f$  by dashed red line with filled circles in Figure 14(a). This immediately reveals the relative strengthening—similar to what is observed in the case of isolated ARs. This experiment with a uniform boost is meant to highlight the necessary correction procedure. Clearly, we need better knowledge of the post-emergence effects on the *f*-mode, not only locally but also in the surrounding medium, to be able to apply a realistic, non-uniform boost that depends on the magnetic activity in the neighborhood.

## 5. IMPLICATIONS

If we accept that  $\tilde{E}_f(t)$  can be used as a precursor to AR formation, we must ask about its possible phys-

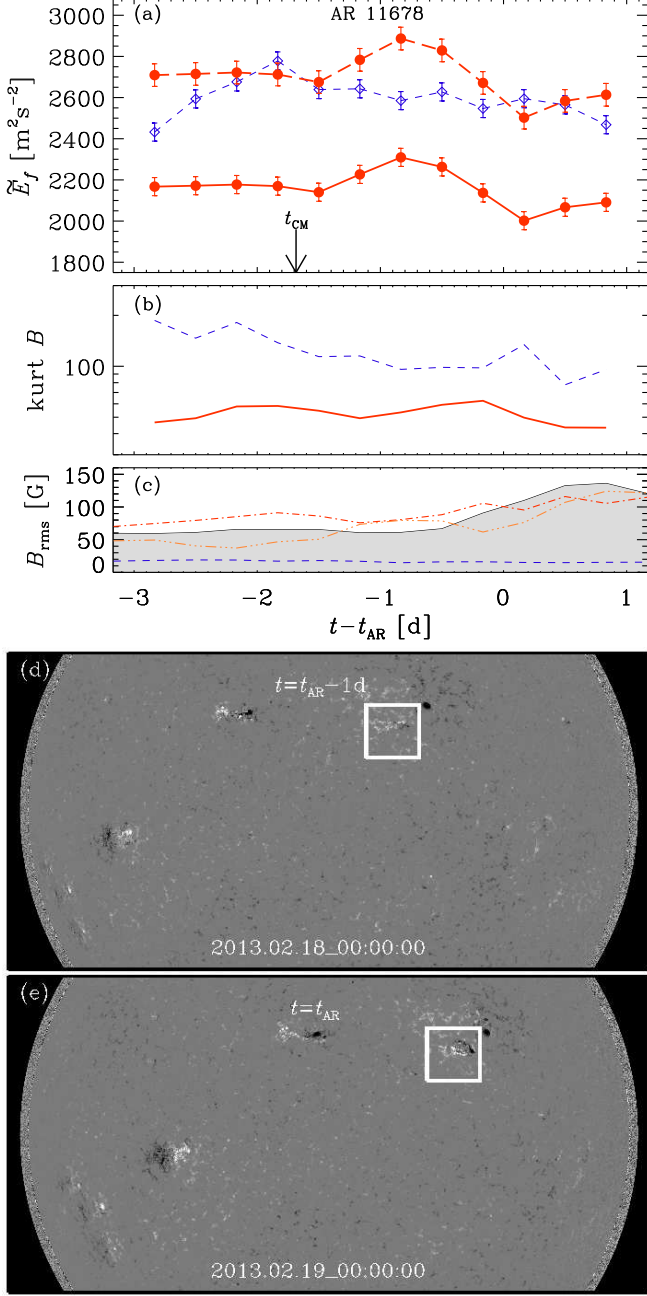


FIG. 14.— Same as Figure 13, but for AR 11678. Here, the dashed (red) line in panel (a) corresponds to  $1.25\tilde{E}_f$ .

ical origin and relevance. Earlier idealized simulations (Singh et al. 2014, 2015) have demonstrated that, while uniform magnetic fields lead to a frequency shift and a weakening of the  $f$ -mode, a nonuniform subsurface field can lead to a fanning and associated strengthening of the  $f$ -mode, provided the magnetic field is at least one or two pressure scale heights below the surface. While such studies should be repeated with more realistic models, they do confront us with the question of how a magnetic field can remain undetected once it is only a few Mm below the surface.

The fact that the  $f$ -mode resides near the top few Mm of the Sun is suggestive of a gradual build-up of the AR

near the surface, instead of a buoyant rise, which would happen in just a few hours (Cheung et al. 2010). This is in stark contrast to the conventional picture of an  $\Omega$ -shaped flux tube rising from the bottom of the convection zone and forming an AR as it pierces the surface (Fan 2001). Earlier simulations of Cheung et al. (2010) with a magnetic field implanted at a depth of nearly 10 Mm below the surface have produced surface manifestations just a few hours later. Such simulations do not address the physics of the *formation* of magnetic flux concentrations. By contrast, several simulations in large enough domains performed by several groups (Stein & Nordlund 2012; Warnecke et al. 2013; Mitra et al. 2014; Käpylä et al. 2016; Masada & Sano 2016) have demonstrated the spontaneous emergence of magnetic flux concentrations right at the surface. This highlights the potential significance of  $f$ -mode-related precursors at constraining our still very sketchy understanding of the solar dynamo (Ossendrijver 2003; Brandenburg 2005; Charbonneau 2010). Yet another important quantity to be investigated in dynamo models is the kurtosis of the magnetic field. Models exhibiting a peak in  $\text{kurt } B$  well before  $B_{\text{rms}}$  saturates are expected to be better constrained and might become more favorable.

## 6. CONCLUSIONS

All six examples of isolated ARs presented in Section 4.1 show that, several days prior to magnetic field emergence, the strength of the  $f$ -mode, as presented by the value of  $\tilde{E}_f$ , rises and then reaches a maximum before displaying the known post-emergence damping. Also, prior to AR emergence, the value of  $\tilde{E}_f$  remains larger for long times with significant energy difference compared to the value obtained from the corresponding quiet sun location,  $(\vartheta^\dagger, \varphi)$ . For the two examples of crowded ARs presented in Section 4.2, however, this is different and, as explained above, the reason for this is in fact expected. We summarise our findings as follows:

- The solar  $f$ -mode is perturbed and shows a strengthening at high wavenumbers caused by the subsurface magnetic fields associated with emerging ARs about 1–2 days before there is any visible magnetic activity in the photosphere. This appears to be independent of the phase within the solar cycle.
- We discussed the wavenumber dependence of the precursor signal and showed that the  $f$ -mode strengthening occurs at fairly large wavenumbers.
- In many cases, the kurtosis of the magnetic field from the patch in which the AR develops shows a peak much before  $B_{\text{rms}}$  from that region saturates.
- As discussed in earlier works, we find that the  $f$ -mode suffers damping after the emergence of the AR.
- The  $f$ -mode strengthening prior to AR formation, followed by its post-emergence damping, are non-local in space, and thus could influence the neighboring patches.

- We proposed a plausible cleaning procedure to extract precursor signal from patches in a crowded environment with one or more pre-existing ARs.

Calculating images of  $\tilde{E}_f$  for the solar disk, as shown by an example in Figure 4, appears to provide explicit information of where the next AR might form. But we need more studies to better understand the post-emergence damping of the  $f$ -mode and its effects on the surrounding medium in order to calibrate the necessary correction/cleaning that must be applied to the data to extract

precursor signals from a polluted medium.

We thank Charles Baldner, Aaron Birch, Rick Bogart, Robert Cameron, Brad Hindman, Maarit Käpylä, Charlie Lindsey, Matthias Rheinhardt, Jesper Schou, Hannah Schunker, Sami Solanki, Junwei Zhao, and the referee for their comments and suggestions. This work has been supported in parts by the Swedish Research Council grant No. 621-2011-5076 as well as a startup grant from CU-Boulder.

## REFERENCES

Birch, A. C., Braun, D. C., & Fan, Y. 2010, *ApJ*, 723, L190  
 Birch, A. C., Schunker, H., Braun, D. C., Cameron, R., Gizon, L., Löptien, B., & Rempel, M. 2016, *Science*, e1600557, pp. 1–6, DOI:10.1126/sciadv.1600557  
 Brandenburg, A. 2005, *ApJ*, 625, 539  
 Brandenburg, A., Kemer, K., Kleeorin, N., Mitra, D., & Rogachevskii, I. 2011, *ApJ*, 740, L50  
 Brandenburg, A., Kleeorin, N., & Rogachevskii, I. 2013, *ApJ*, 776, L23  
 Cally, P. S., Bogdan, T. J., & Zweibel, E. G. 1994, *ApJ*, 437, 505  
 Cally, P. S., & Bogdan, T. J. 1997, *ApJ*, 486, L67  
 Charbonneau, P. 2010, *Living Rev. Solar Phys.*, 7, 3  
 Cheung, M. C. M., Rempel, M., Title, A. M., & Schüssler, M. 2010, *ApJ*, 720, 233  
 Chowdhury, P., Choudhary, D. P., & Gosain, S. 2013, *ApJ*, 768, 188  
 Daiffallah, K., Abdelatif, T., Bendib, A., Cameron, R., & Gizon, L. 2011, *Solar Phys.*, 268, 309  
 Duvall, T. L., Jr., Kosovichev, A. G., & Murawski, K. 1998, *ApJ*, 505, L55  
 Fan, Y. 2001, *ApJ*, 554, L111  
 Felipe, T., Braun, D., Crouch, A., & Birch, A. 2012, *ApJ*, 757, 148  
 Felipe, T., Crouch, A., & Birch, A. 2013, *ApJ*, 775, 74  
 Fernandes, D. N., Scherrer, P. H., Tarbell, T. D., & Title, A. M. 1992, *ApJ*, 392, 736  
 Getling, A. V., Ishikawa, R., & Buchnev, A. A. 2016, *Solar Phys.*, 291, 371  
 Hanasoge, S. M., Birch, A. C., Bogdan, T. J., & Gizon, L. 2008, *ApJ*, 680, 774  
 Ilonidis, S., Zhao, J., & Kosovichev, A. 2011, *Science*, 333, 993  
 Inoue, S., Hayashi, K., Shiota, D., Magara, T., & Choe, G. S. 2013, *ApJ*, 770, 79  
 Käpylä, P. J., Brandenburg, A., Kleeorin, N., Käpylä, M. J., & Rogachevskii, I. 2016, *A&A*, 588, A150  
 Kholkov, S. 2013, *Solar Phys.*, 287, 229  
 Masada, Y., & Sano, T. 2016, *ApJ*, 822, L22  
 Maurya, R. A., Vemareddy, P., & Ambastha, A. 2012, *ApJ*, 747, 134  
 Mitra, D., Brandenburg, A., Kleeorin, N., Rogachevskii, I. 2014, *MNRAS*, 445, 761  
 Murawski, K. and Roberts, B. 1993a, *A&A*, 272, 601  
 Murawski, K. and Roberts, B. 1993b, *A&A*, 272, 595  
 Ossendrijver, M. 2003, *A&A Rev.*, 11, 287  
 Schou, J. 1999, *ApJ*, 523, L181  
 Schrijver, C. J., Aulanier, G., Title, A. M., Pariat, E., & Delannée, C. 2011, *ApJ*, 738, 167  
 Singh, N. K., Brandenburg, A., & Rheinhardt, M. 2014, *ApJ*, 795, L8  
 Singh, N. K., Brandenburg, A., Chitre, S. M., & Rheinhardt, M. 2015, *MNRAS*, 447, 3708  
 Solov'ev, A. A., & Kirichek, E. A. 2009, *ARep*, 53, 675  
 Smirnova, V., Riehokainen, A., Solov'ev, A., Kallunki, J., Zhiltsov, A., & Ryzhov, V. 2013, *A&A*, 552, A23  
 Stein, R. F., & Nordlund, Å. 2012, *ApJ*, 753, L13  
 Sun, X., Hoeksema, J. T., Liu, Y., & Zhao, J. 2015, *ApJ*, 798, 114  
 Thomas, J. H., Cram, L. E., & Nye, A. H. 1982, *Nature*, 297, 485  
 Wachter, R., Schou, J., Rabello-Soares, M. C., Miles, J. W., Duvall, T. L., & Bush, R. I. 2012, *Solar Phys.*, 275, 261  
 Warnecke, J., Losada, I. R., Brandenburg, A., Kleeorin, N., & Rogachevskii, I. 2013, *ApJ*, 777, L37  
 Zhao, J., Chen, R., Hartlep, T., & Kosovichev, A. G. 2015, *ApJ*, 809, L15